water

MDPI

Article

Biochar-Supported Semiconductor Graphitic Carbon Nitride for Visible-Light-Driven Degradation of Triadimefon: Adsorption–Photocatalysis, Mechanism, and Degradation Pathways

Juying Li [1,2,†], Yezhi Dou [2,†], Wei Dai [3], Li Cao [2], Wenzhu Wu [2], Ninghui Song [2], Jia Yu [2], Deyang Kong [2], Cheng Yao [1,*], Feng Ge [2,*] and Kaiping Zheng [4]

[1] School of Chemistry and Molecular Engineering, Nanjing Tech University, Nanjing 211816, China; lijuying@nies.org
[2] Key Laboratory of Pesticide and Emerging Contaminant Environmental Risk Control, Nanjing Institute of Environmental Science, MEE, Nanjing 210042, China; douyezhi@126.com (Y.D.)
[3] Jiangsu Asia Electronics Technology Co., Ltd., Taizhou 225500, China
[4] School of Civil Engineering and Architecture, Wuhan University of Technology, Wuhan 430070, China
* Correspondence: yaocheng@njtech.edu.cn (C.Y.); gefeng@nies.org (F.G.)
† These authors contributed equally to this work.

Abstract

Triadimefon, a broad-spectrum triazole fungicide, has been frequently detected in surface water and soil because of its chemical stability, long residual period, and high mobility, posing potential risks to ecosystems and human health. Conventional treatment technologies are constrained by high costs, low efficiency, and secondary pollution. In this study, a series of biochar/g-C_3N_4 composites (BC/CN-X, X = 5, 10, 20) were fabricated via a facile ultrasonic-assisted route using peanut-shell-derived biochar and graphitic carbon nitride (g-C_3N_4). The adsorption behavior and visible-light photocatalytic degradation performance toward triadimefon of BC/CN-X were systematically investigated. Under visible light, BC/CN-20 degraded 90.6% of triadimefon (500 μg/L) within 20 h, outperforming pristine g-C_3N_4 by 58.3%, and retained a degradation efficiency of 87.6% after four recycling runs. In addition, reaction intermediates were identified using high-resolution HPLC-QTOF-MS, and two degradation pathways were proposed, in which triadimefon was decomposed by the cleavage of the long carbon chain and degradation of the chlorobenzene moiety. In silico toxicity prediction using T.E.S.T. indicated that the degradation proceeds along an overall detoxification trend; however, the transient intermediate M3 was predicted to be more acutely toxic than the parent compound, suggesting that sufficient reaction time should be ensured to achieve its complete conversion in practical applications.

Keywords: triadimefon; visible light; degradation pathways

Check for updates

Academic Editor: Christos S. Akratos

Received: 16 October 2026
Revised: 12 November 2026
Accepted: 16 November 2026
Published: 18 November 2026

Copyright: © 2026 by the authors. Licensee MDPI, Basel, Switzerland. This article is an open access article distributed under the terms and conditions of the Creative Commons Attribution (CC BY) license.

1. Introduction

Triazole fungicides are currently the most widely used broad-spectrum fungicides worldwide [1], whose chemical stability and high environmental mobility have led to frequent detection in surface water and soil, posing non-negligible risks to aquatic ecosystems [2–4]. Triadimefon, as a representative systemic triazole fungicide, has drawn concerns owing to its widespread use and potential hazards to the environment and human beings.

Natural attenuation of triadimefon via hydrolysis, photolysis, and microbial transformation is usually slow and condition-dependent [5,6], proceeding mainly through reduction

to the still-bioactive triadimenol. The stereoisomers of triadimenol differ in persistence and toxicity [7,8], while enantioselective degradation, racemization, and isomerization further complicate residue risk assessment [9–11]. Engineered degradation methods, including biodegradation by isolated strains [12], advanced oxidation processes using TiO_2 photocatalysis [13], and photo-Fenton oxidation [14], have been explored [15]. Nevertheless, such treatments are constrained by high costs, harsh conditions, and secondary pollution. Crucially, current studies mainly focus on removal, leaving the structures and toxicity of transformation products unclarified [14,15]. To conclude, green technologies, applicable under mild conditions, that convert triadimefon into identifiable, low-toxicity products are urgently needed.

Graphitic carbon nitride (g-C_3N_4), a metal-free polymeric semiconductor, has emerged as a promising visible-light photocatalyst owing to its suitable band gap (~2.7–2.8 eV), high physicochemical stability, low cost, and facile preparation [16,17]. Nevertheless, pristine g-C_3N_4 suffers from a small specific surface area, rapid recombination of photogenerated electron–hole pairs, and limited visible-light utilization, which severely restrict its practical activity [18]. Coupling g-C_3N_4 with carbonaceous materials is an effective strategy to overcome these drawbacks: carbon phases can serve as electron acceptors and reservoirs, suppress charge recombination, extend light absorption, and enrich reactants on the catalyst surface [19,20]. Biochar, a porous carbonaceous material produced through the pyrolysis of waste biomass, integrates the merits of abundant feedstock, low cost, large specific surface area, rich surface functional groups, and excellent electron-storage capacity arising from its condensed aromatic structure [21,22]. Loading g-C_3N_4 onto biochar therefore offers dual benefits: biochar not only concentrates target pollutants around the photocatalyst via adsorption but also accepts and shuttles photogenerated electrons, thereby inhibiting electron–hole recombination and boosting the generation of reactive oxygen species [23,24]. Until now, biochar/g-C_3N_4 composites have been broadly applied to photodegrade organic pollutants under visible light [20,25–28]. Notably, most of these studies targeted dyes or antibiotics at ppm-level concentrations. However, their application to triazole fungicides, particularly triadimefon at environmentally relevant sub-ppm concentrations, has rarely been reported, and the associated adsorption–photocatalysis coupling mechanism, degradation intermediates, and ecotoxicological implications remain insufficiently understood.

In this work, a series of biochar/g-C_3N_4 composites (BC/CN-X) were fabricated through a facile ultrasonic-assisted method. Degradation of triadimefon at environmentally relevant sub-ppm levels (0.2–1.2 mg/L) under visible light was carried out, reaching a maximum degradation rate of 90.6% within 20 h. In addition, BC/CN-X composites displayed outstanding stability in reusability tests, and their surface morphology, adsorption kinetics, and isotherms were characterized to unravel the photocatalytic mechanism. Through identification of the degradation intermediates using HPLC-QTOF-MS, two degradation pathways of triadimefon were proposed, complemented by toxicity assessments of the final degradation products using T.E.S.T (Version 5.1.1). This work aims to provide a green and low-cost strategy for treating triadimefon in water and offer mechanistic insight into the degradation process.

2. Materials and Methods

2.1. Chemicals and Reagents

Triadimefon (99.8%) and melamine (99%) were purchased from Aladdin Reagent Co., Ltd. (Shanghai, China). HPLC-grade acetonitrile, methanol, and formic acid were supplied by Merck (Darmstadt, Germany). Ethanol, p-benzoquinone (BQ, 97%), isopropanol (IPA, analytical grade), and ethylenediaminetetraacetic acid disodium salt (EDTA-2Na, analytical grade) were obtained from Macklin Biochemical Co., Ltd. (Shanghai, China). Ultrapure

water (18.2 MΩ·cm) was produced by a Milli-Q system (Millipore, Billerica, MA, USA). Peanut shells, used as the biochar feedstock, were collected from local agricultural waste, air-dried, pulverized, and stored until use.

2.2. Instruments

Surface morphology was observed using scanning electron microscopy (SEM, Zeiss Sigma 300, Carl Zeiss AG, Jena, Germany). Nitrogen adsorption–desorption isotherms, specific surface areas, and pore-size distributions were measured on an ASAP 2460 analyzer (Micromeritics, Norcross, GA, USA). Surface elemental composition and chemical states were analyzed using X-ray photoelectron spectroscopy (XPS, Kratos AXIS Ultra DLD, Shimadzu, Kyoto, Japan). Fourier-transform infrared spectra (FT-IR, Nicolet, Thermo Fisher Scientific, Waltham, MA, USA) were recorded over 500–4000 cm^{-1} at a resolution of 4 cm^{-1}. Crystalline structures were examined by X-ray diffraction (XRD, Bruker D2 Phaser, Madison, WI, USA; Cu target, 10–80°, 2°/min). The optical absorption properties of the samples were analyzed using a UV–Vis–NIR spectrophotometer (UV-3600i Plus, Shimadzu, Kyoto, Japan), and the test wavelength range was 200–800 nm.

2.3. Experimental Procedure

2.3.1. Preparation of Biochar

Peanut shell waste was used as the raw material. After being air-dried and crushed in a pulverizer, the prepared powder was transferred into a crucible, capped, and placed in a muffle furnace at 500 °C for 1 h under the protection of a nitrogen atmosphere, with a heating rate of 5 °C/min. The obtained biochar was then allowed to cool to room temperature, ground through an 80-mesh sieve, and collected for further use. According to basic physicochemical characteristics, the elemental composition of the obtained biochar is 71.91% C, 18.25% O, 1.24% N, and 0.33% S, with an ash content of around 4.56% ± 1.22%. The pH value is about 8.1, and the zeta potential is measured as −17.8 ± 0.9 mV.

2.3.2. Preparation of g-C_3N_4

g-C_3N_4 was prepared through thermal condensation of melamine at 550 °C for 4 h, with a ramp time of 4 h in a muffle furnace. The obtained bulk g- C_3N_4 was then ground into powder using an agate mortar and collected for further use.

2.3.3. Preparation of BC/CN-X Composites

The prepared g-C_3N_4 and biochar were mixed together in a beaker, with mass ratios of 1:5, 1:10, and 1:20. Then, 50 mg of the composites and 100 mL of ultrapure water were added, and the mixture was magnetically stirred for 10 min. The obtained suspension was then sonicated for 24 h, with the temperature maintained at 25 °C (ultrasonication input power: 400 W, power density: 0.56 W cm^{-2}, 40 kHz, 100% duty cycle), followed by centrifugation at 5000 rpm for 20 min. Then, the supernatant was discarded, and the precipitate was collected and dried in an oven at 80 °C. After natural cooling to room temperature, the composite powder was obtained. The prepared photocatalyst was denoted as BC/CN-X (X = 5, 10, 20), which represents the mass ratio of biochar and g-C_3N_4. The compositing step proceeded with essentially complete mass recovery, where virtually all input material was recovered after centrifugation and drying.

2.3.4. Analytical Methods for Triadimefon

Triadimefon was quantified on an Agilent 6475 liquid chromatography–tandem mass spectrometry system (LC–MS/MS) equipped with an electrospray ionization (ESI) source operating in positive-ion mode. Separation was achieved on an Agilent Poroshell 120

EC-C18 column (Agilent Technologies, Inc., Santa Clara, CA, USA; 2.1 × 75 mm, 2.7 μm) at 40 °C with an injection volume of 10 μL and a flow rate of 0.3 mL/min. The mobile phases were 0.1% formic acid in water (A) and methanol (B) with the following gradient: 0–2 min, 80% A; 4 min, 50% A; 6–8 min, 30% A; 10 min, 80% A. The nebulizer gas (N_2) pressure was 0.28 MPa; the drying gas temperature and flow rate were 350 °C and 3 L/min, respectively. Detection was performed in multiple-reaction monitoring (MRM) mode using the transitions m/z 294.1 → 197 (collision energy of 15 eV) and m/z 294.1 → 69 (collision energy of 20 eV), with a dwell time of 200 ms. Calibration standards of 10, 20, 50, 100, 200, and 500 μg/L were prepared in acetonitrile from a 1 mg/L stock solution, and a linear calibration curve was constructed by plotting peak area against concentration. Method validation was performed by spiking ultrapure water at 0.1 and 1.0 mg/L (five replicates per level); after standing for 30 min at room temperature, samples were filtered through 0.22 μm membranes before analysis. Recoveries of 88.6–93.8% with relative standard deviations (RSDs) of 0.9–1.2% were obtained. Note that the 30 min standing mentioned above pertains only to this method-validation recovery test; in the adsorption and photodegradation experiments, sampling was conducted over a period of up to 20 h to ensure adsorption–desorption equilibrium. The limit of detection (LOD) and limit of quantification (LOQ) of the method were [6 and 20 μg/L], respectively; the calibration curve showed good linearity over 10–500 μg/L ($y = 90{,}347x - 1.38$, $R^2 = [0.998]$). The matrix effect was assessed by comparing two calibration series. The first consisted of matrix-matched standards prepared in a blank BC/CN-X suspension, which was processed under identical conditions and at the same dilution factor as the tested samples but without the addition of triadimefon. The second consisted of solvent standards prepared in the mobile phase. The response difference between the two calibration curves did not exceed 15.7%, which is within the ±20% range generally accepted for pesticide-residue quantification (SANTE/11312/2021). The standard calibration curve was used for quantification. Samples with concentrations above the calibration range (e.g., the 0.8 and 1.2 mg/L experiments) were diluted [10-fold] with the mobile phase prior to analysis so that all measurements fell within the calibration range. The recovery of triadimefon in the presence of composite particles was additionally verified to be [93.8~95.1%] with RSDs of 1.2~2.1% Potential interference from dissolved biochar-derived organics was minimized by centrifugation and filtration through 0.22 μm membranes before injection.

2.3.5. Adsorption Kinetics

The adsorption kinetics of BC/CN-X composite materials were studied using the adsorption equilibrium method. To begin with, 1 mg/mL triadimefon stock solutions were prepared using ultrapure water containing 1% acetonitrile as the solvent and then stored in the dark. For the experimental procedure, triadimefon sample solutions were prepared in three parallel groups in 100 mL glass vials by diluting the stock solutions to 50 mL 0.5 mg/L. Then, 20 mg of g- C_3N_4, BC/CN-5, BC/CN-10, and BC/CN-20 were added to each bottle, mixed evenly, and sealed. The sample vials were shaken in the dark at a speed of 200 r/min on a shaker while the temperature was controlled at 20 ± 2 °C. During the reaction process, test samples were taken at 1, 2, 4, 8, 16, and 20 h, and the remaining catalyst could be easily removed by standing and precipitation. The supernatant was then extracted with a pipette, filtered through a 0.22 μm microfiltration membrane, and stored in a brown bottle at −4 °C for further HPLC-MS analysis.

2.3.6. Adsorption Isotherms

Adsorption isotherms were determined by equilibrating 20 mg of each BC/CN-X material with triadimefon solutions of 0.1, 0.3, 0.5, 0.7, 0.9, and 1.1 mg/L for 20 h under

the same conditions. After centrifugation at 8000 r/min for 5 min, the supernatants were filtered and analyzed. Blank experiments without the addition of BC/CN-X (triplicate) confirmed that losses due to volatilization, degradation, and bottle-wall adsorption were below 3%.

2.3.7. Adsorption Calculations

The amount of triadimefon adsorbed by the composite materials was calculated using the following formula:

$$q_t = \frac{(c_i - c_t)V}{m} \quad (1)$$

where q_t (mg/kg) is the adsorbed amount at time t; c_i and c_t (mg/L) are the initial concentration and the concentration at time t of triadimefon, respectively; V (L) is the volume of the solution; and m (kg) is the mass of the material.

The kinetic data were fitted with the pseudo-first-order model (2), the pseudo-second-order model (3), and the Elovich Equation (4):

$$q_t = q_e(1 - e^{-k_1 t}) \quad (2)$$

$$q_t = \frac{k_2 q_e^2 t}{1 + k_2 q_e t} \quad (3)$$

$$q_t = \frac{1}{\beta}\ln(\alpha\beta t + 1) \quad (4)$$

where q_e (mg/kg) is the equilibrium amount of triadimefon adsorbed by the materials, k_1 (1/h) and k_2 (kg/(mg·h)) are the rate constants, and α (mg/kg) and β (kg/mg) are the initial adsorption rate and desorption constants, respectively.

The adsorption isotherm data were fitted with the Freundlich model (5) and the Langmuir model (6):

$$q_t = K_f c_e^n \quad (5)$$

$$q_t = \frac{q_e k c_e}{1 + k c_e} \quad (6)$$

where K_f ((mg/kg)/(mg/L)^n) and n are the Freundlich constants, and c_e (mg/L) is the equilibrium concentration of triadimefon.

2.3.8. Photodegradation Experiments

Photocatalytic experiments were carried out in beakers containing 50 mL of triadimefon solution (500 μg/L) with 20 mg of catalyst under magnetic stirring. A 50 W, 6500 K LED lamp was used as the visible-light source to simulate solar irradiation, which was fixed on top of the solution surface at a distance of 20 cm. The peak emission wavelength range of the lamp was around 400–480 nm, with an average light intensity incident on the suspension surface of 10 mW/cm^2. Prior to irradiation, the suspension was stirred in the dark for 30 min to establish adsorption–desorption equilibrium. Samples of 1 mL were collected at 1, 2, 4, 8, 12, 16, and 20 h, filtered through 0.22 μm membranes, and analyzed by LC–MS/MS. The water level in each beaker was recorded at every sampling event to correct for evaporation. All experiments were performed in triplicate, and the degradation efficiency was calculated as $\eta = (1 - c_t/c_0) \times 100\%$. The effects of catalyst dosage (10, 20, 40, and 60 mg) and initial triadimefon concentration (0.2, 0.4, 0.8, and 1.2 mg/L) were further investigated. To assess reusability, the spent BC/CN-20 was recovered by centrifugation, washed three times with ultrapure water, dried at 60 °C, and reused in four consecutive cycles under identical conditions.

2.3.9. Reactive Species Quenching, Intermediate Identification, and Toxicity Assessment

To identify the reactive species involved in the photocatalytic process, quenching experiments were conducted by adding 1 mmol/L BQ, 2 mmol/L EDTA-2Na, and 0.2 mol/L IPA as scavengers for superoxide radicals ($\cdot O_2^-$), photogenerated holes (h^+), and hydroxyl radicals ($\cdot OH$), respectively. Degradation intermediates were analyzed on a SCIEX X500R QTOF high-resolution LC–MS system(SCIEX, Framingham, MA, USA). Samples collected at 0, 1, 2, and 4 h were separated on an ACQUITY UPLC HSS T3 column (Waters, Milford, MA, USA; 2.1 × 100 mm, 1.8 µm) at 40 °C with methanol (A) and ultrapure water (B) as mobile phases, an injection volume of 5 µL, a flow rate of 0.3 mL/min, and a total run time of 30 min. MS and MS/MS spectra acquired in positive-ion mode were used to elucidate the molecular formulas and structures of the intermediates. Finally, the acute toxicity (oral rat LD_{50}) and developmental toxicity of triadimefon and its degradation products were estimated in silico using the Toxicity Estimation Software Tool (Version 5.1.1).

3. Results

3.1. Characteristics of BC/CN-X

SEM was applied to study the surface morphology of g-C_3N_4 and BC/CN-X, as shown in Figure 1. It can be observed that pure bulk g-C_3N_4 (Figure 1a) displayed a typical heterogeneous bulk structure, which can be attributed to the thermal condensation method. In the SEM images of BC/CN-5, BC/CN-10, and BC/CN-20 (Figure 1b–d), the large surface area and porous structure of the introduced BC can be seen, with the particle size of g-C_3N_4 becoming smaller after sonication and uniformly distributed on the surface of biochar. As the mass of biochar increases, the pores on the surface of the composite materials become larger, and much deeper grooves appear on the surface of BC/CN-20, resulting in a large increase in the specific surface area.

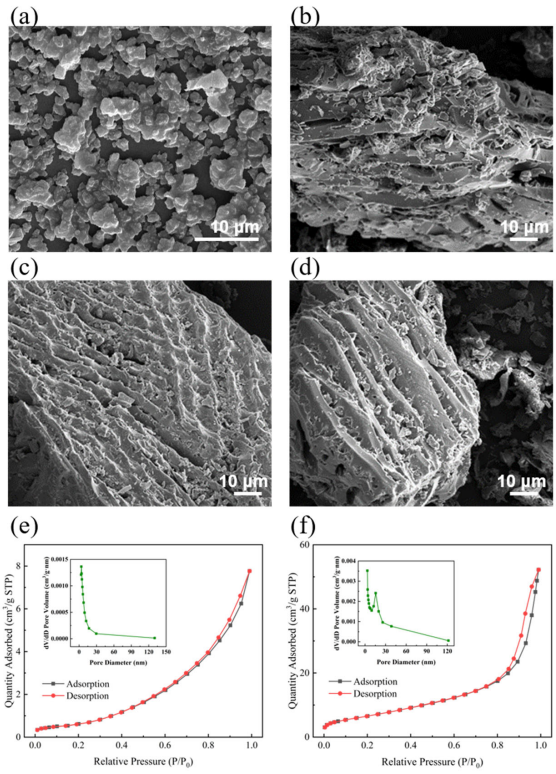


Figure 1. SEM images of (**a**) g-C_3N_4, (**b**) BC/CN-5, (**c**) BC/CN-10, and (**d**) BC/CN-20. N_2 adsorption–desorption isotherms of (**e**) g-C_3N_4 and (**f**) BC/CN-20.

Then, the optical properties of the obtained BC/CN-X were examined using ultraviolet–visible–near-infrared diffuse reflectance spectra (UV–vis DRS), as is displayed and discussed in Figure S1. Briefly, the light absorption ability of BC/CN-X generally improved as the content of biochar increases, suggesting that biochar can reduce light reflection and enable the photocatalyst to absorb a broader range of light wavelengths. Combined with the SEM observation, it can be deduced that the rough surface and abundant porosity of biochar allowed sufficient distribution of g-C_3N_4 in the framework and close adhesion between the composites, thus leading to the potential improvement of electron transfer efficiency because the electron accumulation ability of biochar inhibits electron–hole pair recombination. It is predicted that such composites will easily generate more reactive species and display enhanced photocatalytic activity. In addition, FTIR spectra and XRD were also employed to investigate the functional groups and chemical structures of the obtained composites, which are demonstrated in detail in Figure S2–S4.

3.2. Adsorption Behavior of Triadimefon

3.2.1. BET Specific Area Measurement

To begin with, g-C_3N_4 and BC/CN-20 were selected as BET specific area research objects as they have the most distinct morphology. As shown in Figure 1e,f, the N_2 adsorption–desorption isotherms of g-C_3N_4 and BC/CN-20 were both type IV with H_3 hysteresis loops, indicating irregular mesoporous structures. Pristine g-C_3N_4 showed a specific surface area of 5.353 m^2/g, an average pore diameter of 3.796 nm, and a total pore volume of 0.012 cm^3/g. In contrast, BC/CN-20 exhibited a markedly enlarged specific surface area of 20.099 m^2/g and a total pore volume of 0.077 cm^3/g, which were 3.7 and 6.4 times those of g-C_3N_4, respectively, and an average pore diameter of 3.393 nm. These results confirm that the introduction of biochar and the ultrasonic treatment generated abundant adsorption sites and improved surface texture, consistent with the SEM observations.

3.2.2. Adsorption Kinetics

The adsorption kinetic curves and fitted parameters of triadimefon on the four obtained materials are presented in Figure 2a–c and Table 1. For the three composites, the adsorption process proceeded rapidly within the first 4 h as triadimefon molecules quickly occupied the surface adsorption sites, then slowed down and essentially reached equilibrium at 20 h. The final equilibrium adsorption amounts followed the order BC/CN-20 > BC/CN-10 > BC/CN-5, scaling with the biochar content. Pristine g-C_3N_4 exhibited a markedly lower adsorption rate and amount, and its adsorption rate only began to decline after 12 h, which is attributed to its smaller specific surface area and, consequently, fewer adsorption sites.

The pseudo-first-order model yielded correlation coefficients of 0.839–0.939 (mostly below 0.95), and equilibrium values deviated considerably from the experimental data. In contrast, the pseudo-second-order and Elovich models yielded R^2 values mostly above 0.95, with equilibrium adsorption amounts close to the experimental values, indicating that these two models better describe the adsorption process. The pseudo-second-order model generally represents processes that involve both physisorption and chemisorption, whereas the Elovich model describes heterogeneous diffusion processes with multiple reaction mechanisms. As summarized in Table 1, for all four materials, the pseudo-second-order and Elovich models consistently displayed higher correlation coefficients than the pseudo-first-order model, and the calculated equilibrium adsorption amounts agreed well with the experimental values. It should be noted that the Elovich parameter α is not identifiable once $\alpha\beta t \gg 1$, which holds from the first sampling point onward. Its magnitude is unit-dependent and carries no independent physical meaning. Therefore, the Elovich model is used here only as an empirical descriptor consistent with adsorption

on a heterogeneous surface, and quantitative comparisons among the materials are based on the pseudo-second-order parameters.

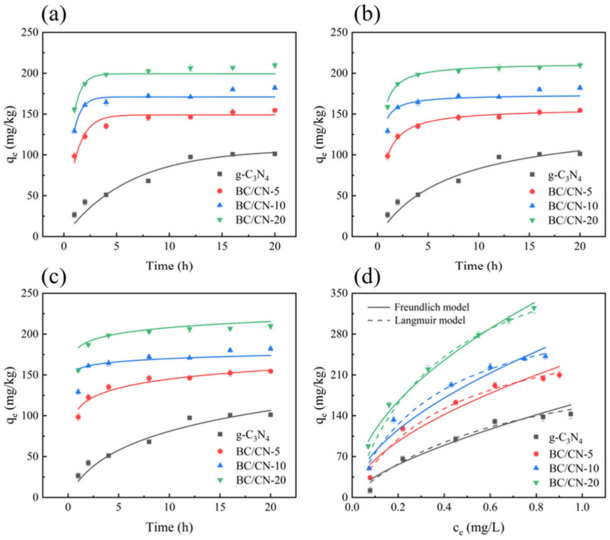


Figure 2. Adsorption kinetic curves of triadimefon on the materials fitted with (**a**) pseudo-first-order, (**b**) pseudo-second-order, and (**c**) Elovich models. (**d**) Adsorption isotherms and fitted curves of triadimefon on the materials. Figures (**a**–**c**) were recorded in the dark at the same catalyst dose (0.4 g/L) and initial concentration (0.5 mg/L) as the photocatalytic tests and therefore also serve as the dark-adsorption controls.

Table 1. Adsorption kinetic parameters of triadimefon on different materials.

Target	Material	Pseudo-First-Order			Pseudo-Second-Order			Elovich		
		q_e	k_1	R^2	q_e	k_2	R^2	α	β	R^2
Triadimefon	g-C_3N_4	107.03	0.16	0.939	142.71	0.01	0.969	25.35	0.02	0.967
	BC/CN-5	148.67	0.93	0.839	157.13	0.01	0.981	1.43×10^4	0.06	0.930
	BC/CN-10	171.09	1.43	0.925	173.89	0.03	0.988	1.08×10^{13}	0.18	0.966
	BC/CN-20	199.67	1.42	0.834	212.42	0.02	0.956	3.00×10^8	0.09	0.983

Note: Elovich α values are reported as fitted parameters only; α is not identifiable in the regime $\alpha\beta t \gg 1$ and is therefore not physically interpreted in this work (see Section 3.2.2).

It is noteworthy that the good fit of both models suggests that the adsorption of triadimefon on the composites may involve both physisorption and chemisorption over a heterogeneous surface. However, kinetic fitting alone cannot directly resolve electron-transfer processes, which require further spectroscopic and electrochemical evidence.

3.2.3. Adsorption Isotherms and Mechanisms

Adsorption isotherms describe the distribution of solute molecules between solid and liquid phases in the equilibrium state. As shown in Figure 2d, the adsorption amounts of all materials increased rapidly at relatively low triadimefon concentrations. When the equilibrium state is reached, BC/CN-20 exhibited the largest adsorption amount, followed by BC/CN-10, BC/CN-5, and pristine g-C_3N_4. At a fixed equilibrium concentration of $c_e \approx 0.9$ mg/L, the measured q_e values were ca. 165, 215, 258, and 330 mg/kg for g-C_3N_4, BC/CN-5, BC/CN-10, and BC/CN-20, respectively (Figure 2d). A tendency toward saturation was observed for BC/CN-5 and BC/CN-10 at the highest concentrations, whereas the isotherm of BC/CN-20 continued to rise, indicating additional uptake capacity; however, none of the isotherms reached a clear plateau within the investigated range.

Both the Freundlich and Langmuir models fitted the data well with $R^2 > 0.92$ (Table 2). Because the measurements were conducted over an environmentally relevant, low concentration range in which saturation was not reached, the Langmuir-fitted q_e values (369.69, 327.37, 346.47, and 416.36 mg/kg for g-C_3N_4, BC/CN-5, BC/CN-10, and BC/CN-20, respectively) represent extrapolated asymptotes rather than directly measured capacities. The associated extrapolation uncertainty is largest for pristine g-C_3N_4, whose data extend to only ca. 45% of its fitted q_e, and whose small affinity constant ($k = 0.83$) leaves the isotherm curvature poorly constrained; its apparently high fitted q_e should therefore not be interpreted as a superior adsorption capacity. Accordingly, the adsorption performance of the materials is ranked in this work by the equilibrium adsorption amounts measured within the investigated concentration range, and the fitted q_e values are reported as model parameters only.

Table 2. Isothermal modelling parameters for adsorption of triadimefon by different materials.

Target	Material	Freundlich Model			Langmuir Model		
		K_f	n	R^2	q_e	k	R^2
Triadimefon	g-C_3N_4	164.24	0.66	0.93	369.69	0.83	0.99
	BC/CN-5	235.32	0.56	0.93	327.37	2.08	0.98
	BC/CN-10	280.51	0.55	0.96	346.47	2.74	0.99
	BC/CN-20	375.29	0.55	0.95	416.36	3.40	0.98

Consistent with this ranking, both the Freundlich constant K_f (Table 2) and the kinetic adsorption amounts (Table 1) increased monotonically with biochar content, confirming that biochar incorporation enhances the adsorption affinity of the composites. The Freundlich heterogeneity factor n decreased with increasing biochar proportion, indicating enhanced surface heterogeneity and more active adsorption sites after the incorporation of biochar. The Freundlich constant K_f of BC/CN-20 (375.29 $(mg/kg)/(mg/L)^n$) was 2.3 times that of pristine g-C_3N_4 (164.24 $(mg/kg)/(mg/L)^n$), demonstrating that biochar significantly improved the surface affinity of the adsorbent.

3.3. Photocatalytic Degradation of Triadimefon

3.3.1. Photocatalytic Activity

The photocatalytic activities of the prepared materials toward triadimefon were evaluated under visible-light irradiation (Figure 3a). Control experiments confirmed that triadimefon underwent no self-degradation in the absence of any catalyst, indicating negligible direct photolysis. It is noteworthy that adsorption and photocatalytic degradation were distinguished by the experimental design: the removal of triadimefon during the initial dark period (Section 2.3.8) corresponded to adsorption alone, whereas further removal after the light was switched on was attributed to photocatalysis. The amount of triadimefon adsorbed onto BC/CN-20 at dark equilibrium was around 210 mg/kg, which is 16.8% of the initial triadimefon amount. Meanwhile, pristine g-C_3N_4 degraded only 32.3% of the original triadimefon within 20 h. In contrast, all BC/CN-X composites outperformed pristine g-C_3N_4, and the degradation efficiency improved with the increased biochar ratio, demonstrating that the presence of biochar effectively enhances photocatalytic performance. BC/CN-20 achieved the highest degradation efficiency of 90.6% within 20 h, an improvement of 58.3% over pristine g-C_3N_4. It should be emphasized that this 90.6% value is the total removal of triadimefon (adsorption + photocatalysis), with the dark-adsorption contribution bounded at ca. 16.8% of the initial amount (ca. 4.2 μg of the initial 25 μg). Therefore, the net photocatalytic degradation amounts to at least ca. 73.8%, and photocatalysis remains the dominant removal mechanism. The superior activity of BC/CN-20 stems from the high porosity and

large specific surface area conferred by biochar, which strengthen triadimefon adsorption and interfacial electron transfer. Furthermore, electron–hole recombination is suppressed, consequently generating more reactive species. Such a deduction is consistent with the structural and optical characterization results above. The photolysis blank is included in Figure 3a, and the corresponding dark-adsorption controls over the full 20 h are presented in Figure 2a–c.

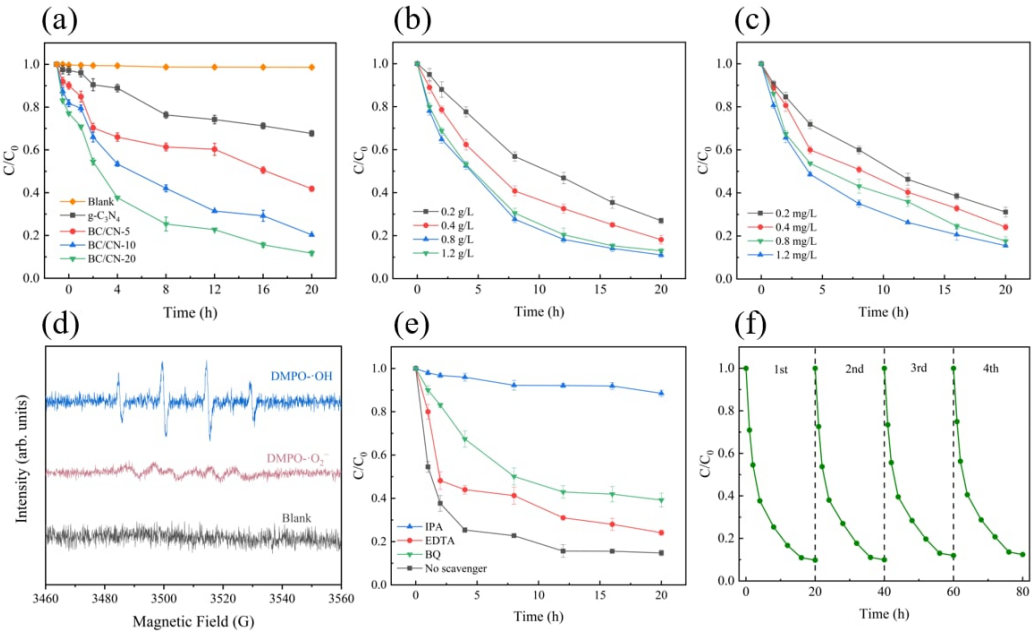


Figure 3. (**a**) Degradation curves of triadimefon by different catalysts under visible light. Effects of (**b**) catalyst dosage and (**c**) initial triadimefon concentration on degradation efficiency. (**d**) EPR experiment of BC/CN-20 under visible light. (**e**) Effect of different scavengers on triadimefon degradation by BC/CN-20. (**f**) Recycling performance of BC/CN-20 for triadimefon degradation. Blank in (**a**): triadimefon solution irradiated without any catalyst (photolysis control).

3.3.2. Effects of Catalyst Dosage and Initial Concentration

As revealed above, BC/CN-20 displayed the most outstanding degradation efficiency out of all of the prepared materials. Thus, in order to gain a better understanding of the proposed degradation system and further inform practical application, the effects of BC/CN-20 dosage (10, 20, 40, and 60 mg) and initial triadimefon concentration are investigated. As shown in Figure 3b, degradation efficiency increased with dosage within the range of 10–40 mg, which may be attributed to the greater accessible surface area and more adsorption/reaction sites when the amount of catalyst is increased. Under these circumstances, concentrated triadimefon molecules around the material may enhance electron transfer. However, after raising the dosage of BC/CN-20 to 60 mg, the corresponding degradation efficiency displayed no further improvement compared with 40 mg, indicating that the adsorption and reaction sites had reached saturation. In addition, excessive suspended particles may shield incident light and attenuate photon utilization. Therefore, 40 mg was identified as the optimal dosage.

The influence of the initial triadimefon concentration (0.2, 0.4, 0.8, and 1.2 mg/L) is presented in Figure 3c. The degradation efficiency within the same reaction time increased with the initial concentration, and all four concentration levels achieved degradation efficiencies above 70% within 20 h. Notably, the 20 h degradation efficiency at 1.2 mg/L differed from that of 0.8 mg/L by only 2.2 percentage points, suggesting that the treatment was possibly reaching optimal loading capacity around 1.2 mg/L. These findings are of

practical significance as most reported studies for removing chlorinated pesticides are performed at the ppm level, which greatly exceeds the concentrations detected in real water bodies. In contrast, the present composite effectively treated triadimefon at sub-ppm levels (0.2–1.2 mg/L), demonstrating its suitability for environmentally relevant scenarios.

3.3.3. Study of Photocatalytic Reactive Species

Studying the photocatalytic mechanism is crucial for understanding the degradation pathway. Therefore, the Electron Paramagnetic Resonance (EPR) test was applied to investigate reactive species during the photodegradation process. The spin radical trap DMPO was used to capture potential reactive species, hydroxyl radicals (·OH), and superoxide radicals (·O2-). As shown in Figure 3d, characteristic EPR signals of DMPO/·OH and DMPO/·$O2^-$ were both determined after irradiating the BC/CN-20 water suspension using visible light. Further quenching experiments were performed to confirm the reactive species responsible for triadimefon degradation (Figure 3e). The addition of all three scavengers suppressed the activity of BC/CN-20 to different extents, following the general order IPA > BQ > EDTA-2Na. Specifically, degradation efficiency dropped from 90.6% (without the scavenger) to 11.5% and 60.8% in the presence of IPA and BQ, respectively, demonstrating that ·OH and ·$O2^-$ are the predominant reactive species in the photocatalytic process. EDTA-2Na also exerted a certain inhibitory effect, suggesting that photogenerated holes (h^+) participate in the reaction to a smaller extent.

3.3.4. Stability and Reusability

Stability and reusability are critical indicators of practical applicability. As shown in Figure 3f, the recycled BC/CN-20 maintained essentially stable photocatalytic activity over consecutive runs. After four recycling cycles, the degradation efficiency of triadimefon remained at 87.6%, only 3% lower than that of the fresh material. This result indicates that the optical properties of the BC/CN-20 composite were well preserved with recycling, highlighting its fine stability, reusability, and economic viability for practical application. In future work, the stability of this material may be further validated through specific characterization techniques, including XPS, XRD, and FTIR, especially under complex, real-world application scenarios.

3.4. Degradation Pathways of Triadimefon and Its Photocatalytic Mechanism

3.4.1. Analysis of Degradation Products

The degradation intermediates of triadimefon were identified using HPLC-QTOF-MS, and samples were collected at 0, 1, 2, and 4 h for analysis. The total ion chromatograms (Figure 4a) show that the parent compound M0 (m/z 293.75) was eluted at 13.62 min. Its peak intensity decreased progressively along with the reaction time, which is in accordance with the degradation test. Additional peaks emerged from 1 h onward, and the corresponding MS and MS/MS spectra (Figure 4b–i) were extracted to elucidate the product structures.

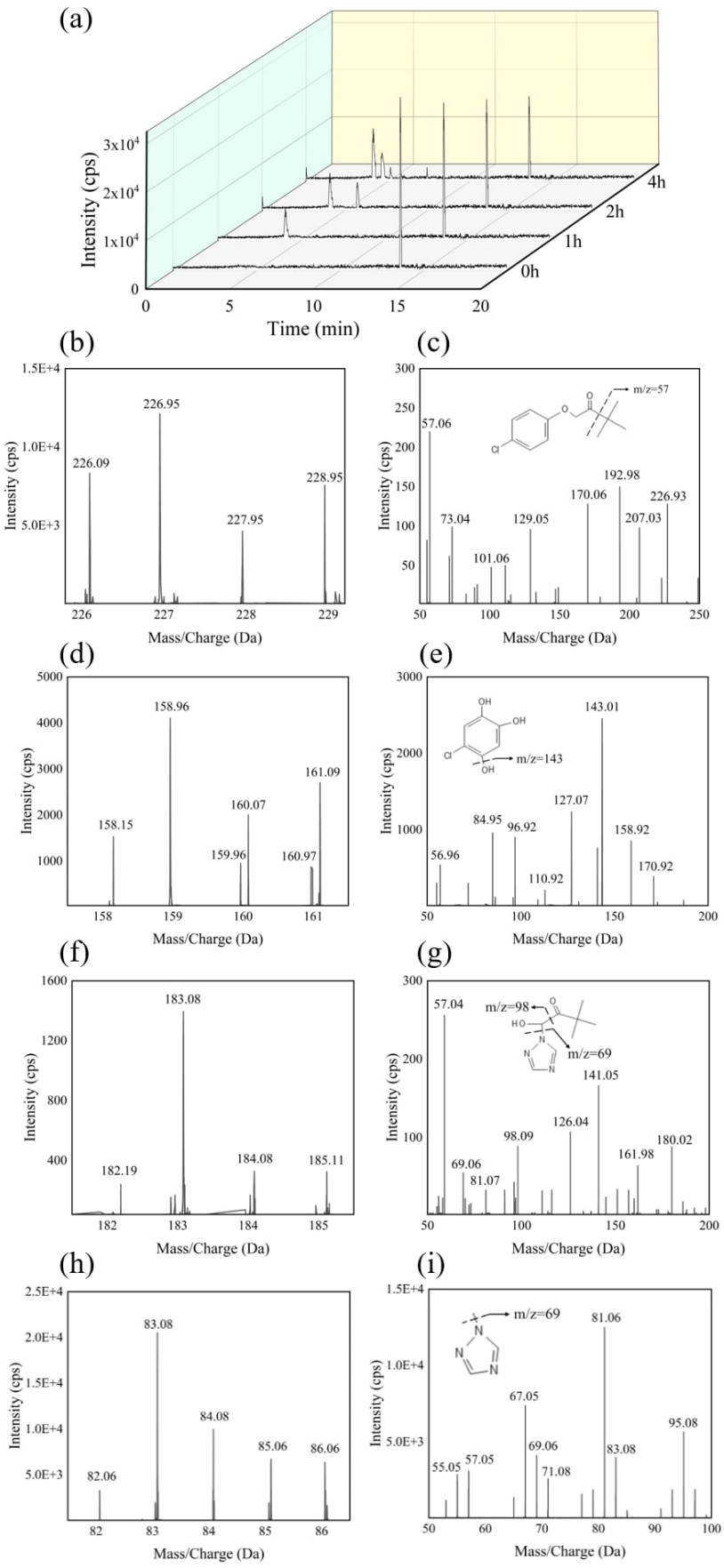


Figure 4. Total ion chromatograms of triadimefon solutions at different irradiation times (**a**) and mass spectra of the triadimefon degradation products M1 (**b**,**c**), M2 (**d**,**e**), M3 (**f**,**g**), and M4 (**h**,**i**).

Product M1 (m/z 226.95) is 66.8 Da lighter than M0, which is consistent with the loss of the triazole moiety. In the MS/MS spectrum, the fragment at m/z 57.06 ($C_4H_9^+$) is diagnostic of the tert-butyl group, indicating that the aliphatic chain remains intact, while the fragment at m/z 129.05 arises from C–O bond cleavage. M1 is therefore tentatively assigned as the detriazolated product of triadimefon, with the molecular formula $C_{12}H_{15}ClO_2$, a structure analogous to 1-(4-chlorophenoxy)-3,3-dimethylbutan-2-one that has been reported as a photolysis product of triadimenol [29,30]. The MS/MS spectrum of product M2 (m/z 158.96, 134.79 Da below M0) shows a prominent fragment at m/z 143.01 (loss of one oxygen), together with fragments at m/z 127.07 and 110.92 corresponding to the loss of two and three oxygens, respectively. Thus, M2 is tentatively assigned as a hydroxylated chlorobenzene with the formula C6H5ClO3, analogous to the hydroxylated chlorobenzenes identified among triadimefon photoproducts [2,31]. Product M3 (m/z 183.08, 110.67 Da below M0) no longer exhibits the chlorine isotopic pattern, indicating the loss of the chlorobenzene moiety. Its MS/MS fragments are at m/z 57.04 (tert-butyl), 69.06 (nitrogen-containing five-membered ring), and 98.09 (loss of the ketone group and tert-butyl group). These results reveal that M3 arises from the cleavage of the C–O bond linking the phenyl ring and could tentatively be assigned the formula of $C_8H_{13}N_3O_2$. Product M4 (m/z 83.08, 210.67 Da below M0) shows no halogen isotopic peaks, and its MS/MS fragments at m/z 57.05, 55.05, and 67.05 contain no diagnostic functional-group ions. Therefore, it is tentatively assigned as a triazole-derived fragment with the formula $C_3H_5N_3$ [29].

All products were detected as protonated molecules [M + H]+ in positive-ESI mode. The theoretical and experimental m/z values, mass errors, and assignment evidence of all products are summarized in Table 3. Because no analytical standards were available for M1–M4, and the mass deviations of these low-abundance signals exceed the ±5 ppm typically achievable for high-intensity ions, the proposed structures are reported as tentative assignments (confidence level 3 according to Schymanski et al. [32]) based primarily on their analogy to literature-reported photoproducts [2,29–31,33]. The degradation pathway shown in Figure 5 should accordingly be regarded as a proposed (tentative) pathway, and the formation sequences (M1→M2 and M3→M4) were inferred from structural relationships rather than from time-resolved signal intensities. In addition, a quantitative isotope-pattern analysis of the archived profile data was performed: the 37Cl isotopologue (M + 2, theoretical relative intensity ca. 32% for one chlorine atom) was not detected above the noise level for either M1 (<2%) or M2 (<1%); the chlorine-containing molecular formulas of M1 and M2 therefore could not be confirmed isotopically, and these assignments rest on the literature analogy discussed above.

Table 3. Identification and deduction of degradation products.

	Formula	Calc. m/z	Obs. m/z	Key Evidence	Conf.
M0	$C_{14}H_{16}ClN_3O_2$	294.1004	294.10	authentic standard; RT 13.62 min	L1
M1	$C_{12}H_{15}ClO_2$	227.0833	226.9503	MS2 57.07 (tert-butyl); literature analog [29,30]	L3
M2	$C_6H_5ClO_3$	159.9927	158.9642	MS2 143.01 140.92 (–H_2O); literature analogs [2,31]	L3
M3	$C_8H_{13}N_3O_2$	183.1008	183.0813	triazole-ring products reported [29,33]	L3
M4	$C_3H_5N_3$	83.0483	83.0851	MS2 57.05, 55.05, 67.05; triazole products reported [29]	L3

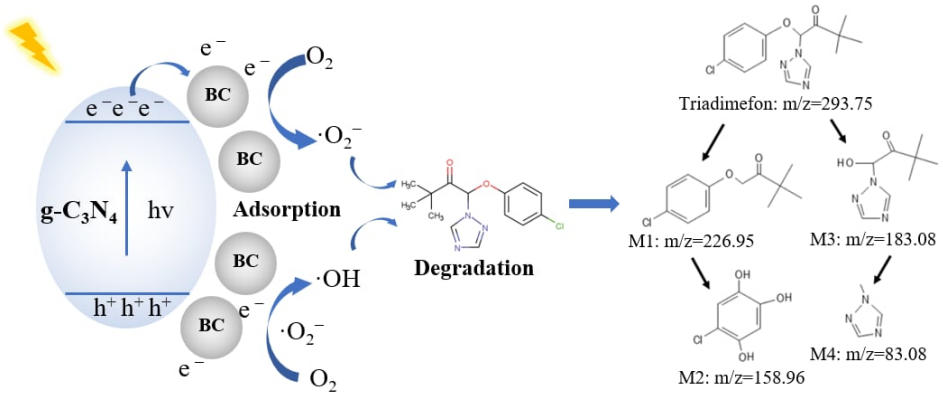


Figure 5. Schematic diagram of the degradation of triadimefon by biochar/g-C3N4 under visible-light irradiation and its proposed (tentative) degradation pathway.

3.4.2. Possible Photocatalytic Mechanism and Degradation Pathways

Based on the above results, a possible mechanism for the visible-light photocatalytic degradation of triadimefon over BC/CN-X composites is proposed (Figure 5). To begin with, under visible-light irradiation, electrons in the valence band of g-C_3N_4 are excited to the conduction band, leaving holes behind and forming electron–hole pairs; in pristine g-C_3N_4, rapid recombination would quickly establish a dynamic equilibrium. The incorporation of biochar breaks this equilibrium by introducing extra surface area and pores, increasing the interfacial contact with g-C_3N_4. Meanwhile, its condensed aromatic structure endows it with strong electron-storage capacity, allowing biochar to act as an electron acceptor that promotes electron transfer from the g-C_3N_4 conduction band and suppresses charge recombination. Consequently, more free electrons and holes are available for subsequent photocatalytic reactions. The photoexcited electrons react with dissolved O_2 and H_2O to generate ·OH and ·$O2^-$, which attack triadimefon molecules and degrade them into smaller products. Furthermore, the valence-band holes may also contribute to direct oxidation. The degradation of triadimefon is deduced to proceed through two pathways. In pathway I (cleavage of the long carbon chain), triadimefon will lose the triazole ring to form M1 first, and the remaining chlorophenyl structure is subsequently hydroxylated and oxidized to M2. In pathway II (degradation of the chlorobenzene moiety), the C–O bond connecting the chlorophenyl group is cleaved to yield M3, which is further degraded into the low-molecular-weight nitrogen-containing heterocycle M4. Both pathways converge toward smaller, less chlorinated molecules, indicating progressive detoxification of the parent fungicide under the attack of ·OH and ·$O2^-$. Meanwhile, the strong adsorption capability of biochar enriches triadimefon around the photocatalyst, raising the local substrate concentration in the photocatalytic zone and accelerating the reaction.

This interpretation is further supported by photoluminescence (PL) measurements. Pristine g-C_3N_4 displays a broad emission band over 400–550 nm, whereas the PL emission of all three BC/CN-X composites was quenched to below the detection limit, exhibiting only near-baseline emission (Figure S5). Since the g-C_3N_4 framework remains intact in the composites (Figures S2 and S3), the observed PL quenching indicates that radiative electron–hole recombination is effectively suppressed after biochar incorporation, which is consistent with the proposed role of biochar as an electron acceptor that promotes charge separation [25].

3.5. Toxicity Assessment of the Degradation Products

To evaluate whether the degradation process introduces additional environmental risks, the acute toxicity (oral rat LD_{50}) and developmental toxicity of triadimefon and

its products were estimated using the T.E.S.T. software based on the putative (tentative) product structures, and the results therefore represent conservative estimates (Table S1 and Figure 6). Regarding acute toxicity, among the four products, only M3 was classified as "very toxic", with the oral rat LD_{50} predicted to be 527.34 mg/kg. M1, M2, and M4 were categorized as "toxic", with M4 showing the lowest toxicity, displaying a predicted LD_{50} of 2178.13 mg/kg. In terms of developmental toxicity, only M3 exhibited a developmental toxicity flag, while the other products were comparable to the parent M0. Importantly, the degradation pathway analysis shows that M3 is an intermediate that is further converted into the much less toxic M4, indicating that the overall transformation proceeds toward reduced toxicity. These results suggest that the photocatalytic treatment developed in this study does not aggravate the environmental hazard risk of triadimefon and can be regarded as a clean and green technology. It should be noted that T.E.S.T. is an in silico QSAR-based prediction tool, and the predicted toxicity trends should be further validated using experimental bioassays. In particular, ecotoxicological tests on actual post-reaction mixtures using aquatic organisms (e.g., *Daphnia magna*) before the process and after 4, 8, and 20 h of exposure would be required to confirm detoxification, since the products may interact synergistically. Nevertheless, given the transient formation of the more acutely toxic M3, reaction conditions should be optimized in practical applications to ensure sufficient conversion of this intermediate. Specifically, the reaction time in practical applications should extend beyond the depletion of the parent compound to ensure complete conversion of M3. Under the conditions of this study, the full 20 h irradiation protocol meets this requirement, and monitoring of M3 (e.g., by LC–MS) is recommended as the practical endpoint criterion when applying the process.

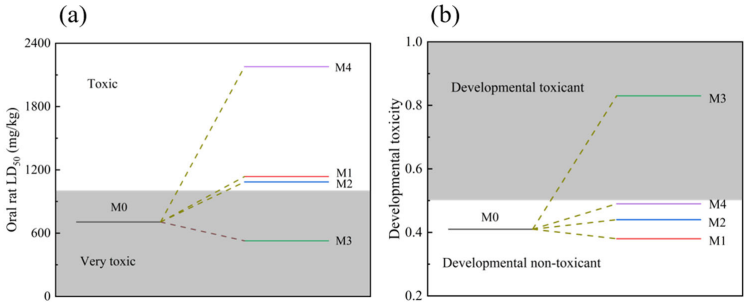


Figure 6. Toxicity assessment of triadimefon and its degradation products: (**a**) acute toxicity and (**b**) developmental toxicity.

4. Discussion

In this study, a series of biochar/g-C_3N_4 composites (BC/CN-X, X = 5, 10, 20) were successfully fabricated via a facile ultrasonic-assisted route using peanut-shell-derived biochar. The adsorption behavior and visible-light photocatalytic performance toward triadimefon of BC/CN-X were systematically demonstrated. Specifically, BC/CN-20 achieved a total removal of up to 90.6% of triadimefon within 20 h under the irradiation of visible light and maintained an efficiency of 87.6% after four recycling runs. Notably, efficient removal (>70%) was achieved at environmentally relevant sub-ppm levels (0.2–1.2 mg/L). EPR and quenching experiments identified ·OH and $\cdot O2^-$ as the predominant reactive species, with photogenerated holes playing a minor role. Through further analysis of degradation intermediates using HPLC-QTOF-MS, two possible degradation pathways were proposed: 1. detriazolation followed by hydroxylation/oxidation of the chlorophenyl moiety, and 2. C–O bond cleavage followed by heterocycle degradation. Both pathways converge on triadimefon to smaller, less chlorinated products. T.E.S.T. toxicity prediction suggested

that the overall transformation proceeds toward reduced toxicity, demonstrating that this treatment is environmentally friendly. Nevertheless, the transient formation of the more acutely toxic intermediate M3 calls for sufficient reaction time in practice. Overall, this work provides a green, reusable strategy based on low-cost waste biomass feedstock for visible-light detoxification of triadimefon and highlights the promise of biochar-supported photocatalysts for treating pesticide residues at environmentally relevant concentrations. Future efforts may shed light on performance validation in real water matrices, evaluation of mineralization efficiency, and pilot-scale application. In practice, the spent catalyst is readily recovered from suspension by centrifugation or filtration, and immobilization of the composite on membranes or monolithic supports represents an engineering route toward continuous-flow application. In addition, experimental bioassays on post-reaction mixtures (e.g., *Daphnia magna* at 0, 4, 8, and 20 h of irradiation), time-resolved semi-quantitative profiling of the degradation products, photon-flux-normalized quantum-efficiency measurements, structural and surface characterization of the spent catalyst after recycling (XRD, FTIR, and XPS), energy-footprint assessment of the synthesis, and tests in real-life water matrices should be further investigated in future work.

Supplementary Materials: The following supporting information can be downloaded at: https://www.mdpi.com/article/10.3390/w18222879/s1, Supplementary Information: Figure S1: UV–vis absorption and Tauc plots (band-gap analysis) of g-C_3N_4 and BC/CN-X; Figure S2: FTIR spectra of g-C3N4 and BC/CN-X; Figure S3: XRD patterns of g-C_3N_4 and BC/CN-X; Figure S4: XPS spectra of g-C_3N_4 and BC/CN-20: (a) C 1s, (b) N 1s, and (c) O 1s; Figure S5: Photoluminescence emission spectra of g-C_3N_4 and BC/CN-X. Table S1: T.E.S.T.-predicted acute toxicity (oral rat LD_{50}) and developmental toxicity of triadimefon (M0) and its tentative degradation products (M1–M4).

Author Contributions: Conceptualization, J.L., Y.D., C.Y. and F.G.; methodology, J.L., W.D., J.Y., K.Z. and W.D.; software, Y.D., L.C., N.S. and D.K.; validation, W.D., L.C. and N.S.; formal analysis, W.D., W.W. and D.K.; investigation, L.C., W.W., J.Y., K.Z. and W.D.; resources, J.L., N.S., D.K., K.Z. and W.D.; data curation, W.W. and N.S.; writing—original draft preparation, J.L. and J.Y.; writing—review and editing, Y.D., J.Y., K.Z. and W.D.; visualization, L.C., W.W. and D.K.; supervision, W.D., C.Y. and F.G.; project administration, J.L., Y.D. and F.G.; funding acquisition, Y.D., C.Y. and F.G. All authors have read and agreed to the published version of the manuscript.

Funding: This research received no external funding.

Data Availability Statement: The original contributions presented in this study are included in the article/Supplementary Material. Further inquiries can be directed to the corresponding authors.

Acknowledgments: The authors have reviewed and edited the output and take full responsibility for the content of this publication.

Conflicts of Interest: One author (Wei Dai) is currently employed by Jiangsu Asia Electronics Technology Co., Ltd., but this study was performed while he was affiliated with the Nanjing Institute of Environmental Science. The company had no role in study design, data collection, analysis, interpretation of data, manuscript writing, or the decision to submit for publication, and no financial or material support was obtained from the company for this work.

References

1. Zhang, W.; Teng, M.; Chen, L. A review on the enantioselective distribution and toxicity of chiral pesticides in aquatic environment. *Environ. Geochem. Health* **2024**, *46*, 317. [CrossRef] [PubMed]
2. Hou, L.; Jin, X.; Liu, N.; Luo, Y.; Yan, Z.; Chen, M.; Liu, Y.; Xie, H.; Giesy, J.P.; Wu, F.; et al. Triadimefon in aquatic environments: Occurrence, fate, toxicity, and ecological risk. *Environ. Sci. Eur.* **2022**, *34*, 12. [CrossRef]
3. Liu, N.; Jin, X.; Zhou, J.; Wang, Y.; Yang, Q.; Wu, F.; Giesy, J.P.; Johnson, A.C. Predicted no-effect concentration (PNEC) and assessment of risk for the fungicide, triadimefon based on reproductive fitness of aquatic organisms. *Chemosphere* **2018**, *207*, 682–689. [CrossRef] [PubMed]

4. Wang, Y.; Ren, Y.; Ning, X.; Li, G.; Sang, N. Environmental exposure to triazole fungicide causes left-right asymmetry defects and contributes to abnormal heart development in zebrafish embryos by activating PPARγ-coupled Wnt/β-catenin signaling pathway. *Sci. Total Environ.* **2023**, *859*, 160286. [CrossRef] [PubMed]
5. Singh, N. Factors Affecting Triadimefon Degradation in Soils. *J. Agric. Food Chem.* **2005**, *53*, 70–75. [CrossRef] [PubMed]
6. Sun, X.; Yang, G.; Cao, X.; Lin, Z. Photochemical degradation of triadimefon in seawater. *J. Ocean Univ. China* **2008**, *7*, 171–176. [CrossRef]
7. Xu, P.; Huang, L. Stereoselective bioaccumulation, transformation, and toxicity of triadimefon in Scenedesmus obliquus. *Chirality* **2016**, *29*, 61–69. [CrossRef] [PubMed]
8. Garrison, A.W.; Avants, J.K.; Jones, W.J. Microbial Transformation of Triadimefon to Triadimenol in Soils: Selective Production Rates of Triadimenol Stereoisomers Affect Exposure and Risk. *Environ. Sci. Technol.* **2011**, *45*, 2186–2193. [CrossRef] [PubMed]
9. Li, Z.; Zhang, Y.; Li, Q.; Wang, W.; Li, J. Enantioselective Degradation, Abiotic Racemization, and Chiral Transformation of Triadimefon in Soils. *Environ. Sci. Technol.* **2011**, *45*, 2797–2803. [CrossRef] [PubMed]
10. Katagi, T. Isomerization of chiral pesticides in the environment. *J. Pestic. Sci.* **2012**, *37*, 1–14. [CrossRef]
11. Kong, Z.; Quan, R.; Fan, B.; Liao, Y.; Chen, J.; Li, M.; Dai, X. Stereoselective behaviors of the fungicide triadimefon and its metabolite triadimenol during malt storage and beer brewing. *J. Hazard. Mater.* **2020**, *400*, 123238. [CrossRef] [PubMed]
12. Wang, Y.; Guan, Q.; Jiao, W.; Li, J.; Zhao, R.; Zhang, X.; Fan, W.; Wang, C. Isolation, identification and transcriptome analysis of triadimefon-degrading strain *Enterobacter hormaechei* TY18. *Biodegradation* **2024**, *35*, 551–564. [CrossRef] [PubMed]
13. Reddy, K.S.N.; Hisanaga, T.; Tanaka, K. Photodegradation of fungicide triadimefon and pesticide pirimicarb in aqueous TIO_2 suspension. *Toxicol. Environ. Chem.* **1999**, *68*, 403–412. [CrossRef]
14. Gkorgkolia, C.; Fytianos, K. Degradation of the Endocrine-Disrupting Compound Triadimenol Using Photo-Fenton Reaction System and Experimental Design. *Water Air Soil Pollut.* **2023**, *234*, 57. [CrossRef]
15. Rachna; Singh, M.P.; Goswami, S.; Singh, U.K. Pesticide pollution: Toxicity, sources and advanced remediation approaches. *Environ. Sci. Pollut. Res.* **2024**, *31*, 64385–64418. [CrossRef] [PubMed]
16. Wang, X.; Maeda, K.; Thomas, A.; Takanabe, K.; Xin, G.; Carlsson, J.M.; Domen, K.; Antonietti, M. A metal-free polymeric photocatalyst for hydrogen production from water under visible light. *Nat. Mater.* **2008**, *8*, 76–80. [CrossRef] [PubMed]
17. Ong, W.-J.; Tan, L.-L.; Ng, Y.H.; Yong, S.-T.; Chai, S.-P. Graphitic Carbon Nitride ($g\text{-}C_3N_4$)-Based Photocatalysts for Artificial Photosynthesis and Environmental Remediation: Are We a Step Closer To Achieving Sustainability? *Chem. Rev.* **2016**, *116*, 7159–7329. [CrossRef] [PubMed]
18. Yu, X.; Ng, S.F.; Putri, L.K.; Tan, L.L.; Mohamed, A.R.; Ong, W.J. Point-Defect Engineering: Leveraging Imperfections in Graphitic Carbon Nitride ($g\text{-}C_3N_4$) Photocatalysts toward Artificial Photosynthesis. *Small* **2021**, *17*, 2006851. [CrossRef] [PubMed]
19. Liu, J.; Zou, R.; Zhang, H.; Song, Y.; Liu, Y.; Yang, S.; Xia, R.; Iwuoha, E.I.; Feleni, U.; Admassie, S.; et al. Enhanced π-electron transport in graphitic carbon nitride ($g\text{-}C_3N_4$) by constructing biochar-welded donor-acceptor (D-A) configuration for photocatalytic conversion of biomass. *Appl. Catal. B Environ. Energy* **2024**, *357*, 124312. [CrossRef]
20. Wang, H.; Guo, W.; Si, Q.; Liu, B.; Zhao, Q.; Luo, H.; Ren, N. Multipath elimination of bisphenol A over bifunctional polymeric carbon nitride/biochar hybrids in the presence of persulfate and visible light. *J. Hazard. Mater.* **2021**, *417*, 126008. [CrossRef] [PubMed]
21. Dai, Y.; Zhang, N.; Xing, C.; Cui, Q.; Sun, Q. The adsorption, regeneration and engineering applications of biochar for removal organic pollutants: A review. *Chemosphere* **2019**, *223*, 12–27. [CrossRef] [PubMed]
22. Patel, A.K.; Singhania, R.R.; Pal, A.; Chen, C.-W.; Pandey, A.; Dong, C.-D. Advances on tailored biochar for bioremediation of antibiotics, pesticides and polycyclic aromatic hydrocarbon pollutants from aqueous and solid phases. *Sci. Total Environ.* **2022**, *817*, 153054. [CrossRef] [PubMed]
23. Pi, L.; Jiang, R.; Zhou, W.; Zhu, H.; Xiao, W.; Wang, D.; Mao, X. $G\text{-}C_3N_4$ Modified biochar as an adsorptive and photocatalytic material for decontamination of aqueous organic pollutants. *Appl. Surf. Sci.* **2015**, *358*, 231–239. [CrossRef]
24. Bhavani, P.; Hussain, M.; Park, Y.-K. Recent advancements on the sustainable biochar based semiconducting materials for photocatalytic applications: A state of the art review. *J. Clean. Prod.* **2022**, *330*, 129899. [CrossRef]
25. Tang, R.; Gong, D.; Deng, Y.; Xiong, S.; Zheng, J.; Li, L.; Zhou, Z.; Su, L.; Zhao, J. π-π stacking derived from graphene-like biochar/$g\text{-}C_3N_4$ with tunable band structure for photocatalytic antibiotics degradation via peroxymonosulfate activation. *J. Hazard. Mater.* **2022**, *423*, 126944. [CrossRef] [PubMed]
26. Wang, T.; Zheng, J.; Cai, J.; Liu, Q.; Zhang, X. Visible-light-driven photocatalytic degradation of dye and antibiotics by activated biochar composited with K^+ doped $g\text{-}C_3N_4$: Effects, mechanisms, actual wastewater treatment and disinfection. *Sci. Total Environ.* **2022**, *839*, 155955. [CrossRef] [PubMed]
27. Luo, S.; Li, S.; Zhang, S.; Cheng, Z.; Nguyen, T.T.; Guo, M. Visible-light-driven Z-scheme protonated $g\text{-}C_3N_4$/wood flour biochar/$BiVO_4$ photocatalyst with biochar as charge-transfer channel for enhanced RhB degradation and Cr(VI) reduction. *Sci. Total Environ.* **2022**, *806*, 150662. [CrossRef] [PubMed]

28. Xiao, L.; Zhang, S.; Chen, B.; Wu, P.; Feng, N.; Deng, F.; Wang, Z. Visible-light photocatalysis degradation of enrofloxacin by crawfish shell biochar combined with g-C_3N_4: Effects and mechanisms. *J. Environ. Chem. Eng.* **2023**, *11*, 109693. [CrossRef]
29. Clark, T.; Watklns, D.A.M. Photolysis of triadimenol. *Chemosphere* **1986**, *15*, 765–770. [CrossRef]
30. Iesce, M.R.; Graziano, M.L.; Cermola, F.; Montella, S.; di Gioia, L.; Stasio, C. Effects of sensitizers on the photodegradation of the systemic fungicide triadimenol. *Chemosphere* **2003**, *51*, 163–166. [CrossRef] [PubMed]
31. Moza, P.N.; Hustert, K.; Feicht, E.; Kettrup, A. Comparative rates of photolysis of triadimefon in aqueous solution in the presence of humic and fulvic acid. *Chemosphere* **1995**, *30*, 605–610. [CrossRef]
32. Schymanski, E.L.; Jeon, J.; Gulde, R.; Fenner, K.; Ruff, M.; Singer, H.P.; Hollender, J. Identifying Small Molecules via High Resolution Mass Spectrometry: Communicating Confidence. *Environ. Sci. Technol.* **2014**, *48*, 2097–2098. [CrossRef] [PubMed]
33. Ni, Z.; Chen, Z.; Zhang, X.; Yang, X.; Zhou, L. Photolysis of fungicide triadimefon: A combined experimental and theoretical investigation on homolytic C O and C N bonds dissociation mechanisms. *J. Photochem. Photobiol. A Chem.* **2023**, *436*, 114402. [CrossRef]

Disclaimer/Publisher's Note: The statements, opinions and data contained in all publications are solely those of the individual author(s) and contributor(s) and not of MDPI and/or the editor(s). MDPI and/or the editor(s) disclaim responsibility for any injury to people or property resulting from any ideas, methods, instructions or products referred to in the content.